Remote Sensing of Environment 265 (2021) 112653

Contents lists available at ScienceDirect

Remote Sensing of Environment

journal homepage: www.elsevier.com/locate/rse

# Diffraction of irregular ocean waves measured by altimeter in the lee of islands

Nelson Violante-Carvalho [a,*], Wilton Z. Arruda [b], Luiz Mariano Carvalho [c], W. Erick Rogers [d], Marcello Passaro [e]

[a] Ocean Engineering Program, Rio de Janeiro Federal University, Rio de Janeiro, Brazil
[b] Mathematics Institute, Rio de Janeiro Federal University, Rio de Janeiro, Brazil
[c] Department of Applied Mathematics, Rio de Janeiro State University, Rio de Janeiro, Brazil
[d] Naval Research Laboratory, Stennis Space Center, MS, USA
[e] Deutsches Geodatisches Forschungsinstitut (DGFI-TUM), Munich, Germany

ARTICLE INFO

Editor: Dr. Menghua Wang

*Keywords:*
Water wave diffraction
Coastal altimetry
Retracked altimeter data
Significant wave height
JASON-2
Wave propagation

ABSTRACT

Despite the importance of diffraction of irregular ocean waves, there is a lack of reported measurements over scales larger than a few tens of wavelengths. In the coastal zone, Satellite Altimetry is hindered because the backscatter characteristics of waveforms deviate from Brown's theoretical model, specially up to 20 km from the coastline. Here, we combine a novel set of retracked — reprocessed — altimeter data with directional buoy spectra and simulations with a spectral numerical model where diffraction is computed with an approximation based on the Mild Slope Equation. The Channel Islands, off the coast of California, is an ideal spot for the analysis because of the sharp variations in bathymetry in the vicinity of the archipelago, increasing the relative importance of diffraction over refraction. Spatial variations of wave energy in the lee of the islands are investigated along and across the wave propagation direction. For the first time the lateral rate of energy spreading — across the wave propagation direction — was computed in oceanic conditions and are of the same magnitude as those found in previously published experiments in a wave tank. The importance of diffraction as a non-dissipative process during wave propagation in situations normally encountered in the ocean is also discussed.

## 1. Introduction

The process of diffraction experienced by water waves is similar to the diffraction of light and sound, regarding their different wavelengths. In the water, diffraction occurs whenever there is a gradient of wave height along the direction perpendicular to the wavenumber vector, therefore along a line of constant phase. An intuitive — and particularly significant — example is that of waves encountering an emerged obstacle, such as a breakwater or an island, when they bend and change direction propagating into the sheltered area according to the Huygens-Fresnel principle. However, a gradient of wave height along a crest can also be generated by refraction (Vincent and Briggs, 1989) or because of the short-crestedness of the wave itself (Babanin and Waseda, 2015). Therefore, diffraction is ubiquitous in the ocean, with diverse levels of activity that are time and/or space dependent.

Employing concepts of optical diffraction, Sommerfeld (1896) proposed solutions for light, sound and electromagnetic waves, which were later adapted for water waves (Penny and Price, 1952). Theoretically, the simplest approach is to consider regular waves propagating in deep water interacting with a semi-infinite breakwater, when analytical solutions are available — see a review in McCormick and Kraemer (2002). For longer crests, the shadow zone spreads further in the lee of the obstacle. However, directional spreading observed in irregular waves, much more common in the ocean, strongly affects diffraction. For short-crested waves with broad directional spreading, the effects of diffraction increase energy in the lee of a breakwater when compared with long-crested, quasi-unidirectional waves (Goda et al., 1978; Briggs et al., 1995).

Numerically, diffraction can only be strictly represented by phase-resolving models, in general based on the Boussinesq Equation (Peregrine, 1967) or on the Mild Slope Equation (MSE — Berkhoff, 1972). These models are computationally demanding — they must have so many grid points per wavelength which is severely burdensome when representing both long and short waves in a single modeling system —

* Corresponding author.
*E-mail address:* n_violante@oceanica.ufrj.br (N. Violante-Carvalho).

https://doi.org/10.1016/j.rse.2021.112653
Received 4 November 2020; Received in revised form 9 August 2021; Accepted 16 August 2021
Available online 26 August 2021

and their use is in general restricted to relatively small spatial domains. Spectral, phase-averaged models described by the Hasselmann equation (Hasselmann, 1962), have the advantage of being more efficient in large-scale computations. The effect of refraction is readily accounted for, as well as the physical processes generally not included in phase-resolving models — such as energy generation, dissipation and wave–wave interactions. Diffraction, on the other hand, can only be simulated through numerical diffusion, with some constraints (Resio, 1987, 1988). Alternatively, some spectral models include an approximation to compute diffraction, where the effect of bending direction is based on the MSE — referred as phase-decoupled models (Holthuijsen et al., 2003; Janssen et al., 2008; Liau et al., 2011; Fang et al., 2019) — improving their overall accuracy (Ilic et al., 2007; Rusu et al., 2008; Toledo and Agnon, 2009; Kim et al., 2017; Do et al., 2020).

Traditionally, diffraction has been treated mainly as an engineering problem. Designers of harbours have been using diffraction diagrams since the 1960's (Wiegel, 1962) assuming the incidence of monochromatic waves, resulting in significant underestimation of energy behind obstacles. This principle was later extrapolated applying the solution for monochromatic waves to an estimated directional wave spectrum assumed as the composition of a limited number of regular waves. Currently, numerical models are undoubtedly useful for studying complex projects employing diverse wave conditions and energy absorbing materials, as long as the embedded theories are supported by measurements in real situations. Moreover, diffraction has been receiving additional attention because of the recent world-wide implementation of wave energy converters, impacting coastal conditions down-wave (Abanades et al., 2015).

The scientific relevance of diffraction is of broader importance to physical oceanography, such as in studies of beach morphodynamics (Elshinnawy et al., 2018), long-distance changes in wave direction behind islands (de León and Guedes Soares, 2005) and the effects on infragravity waves (Mendes et al., 2020). Its role on swell propagation, to name an additional example, is yet not clear. The pioneering work by Snodgrass et al. (1966) demonstrated that waves can propagate thousands of kilometres with little attenuation. More recently, combining satellite measurements and numerical models, several investigations have examined swell evolution and dissipation over large distances (Collard et al., 2009; Ardhuin et al., 2009; Young et al., 2013; Jiang et al., 2016). Energy reduction is associated with dissipative (such as turbulence) and non-dissipative (such as directional spreading, frequency dispersion, diffraction) processes. Diffraction of irregular waves in the ocean is, indisputably, the least studied of them all. It is also unquestionable that swell forecasts in state of the art numerical models are still poor represented, when compared with the windsea part of the spectrum.

Wave crests are finite, no matter whether in deep or shallow water or for windsea or swell, therefore subject to diffraction along their propagation — hence their heights are accordingly expected to be gradually reduced. Experiments in wave tanks point out that the magnitudes of the rate of lateral transmission of energy along crests are too high to be consistent with what is observed in the ocean (Babanin and Waseda, 2015). The presence of background wave energy might inhibit or totally interrupt the rate of reduction caused by diffraction, which could explain the reported discrepancies. Additionally, those authors also proposed relations for the rate of lateral energy migration that are proportional to wave steepness — in tanks the wave steepness can be two orders of magnitude smaller than those normally encountered in the ocean. That also raises questions about the feasibility of extrapolating their experimental results to the real ocean. Measurements of diffracted waves in the ocean over sufficiently long distances to infer the rate of lateral energy migration are non-existent so far, to the best of our knowledge.

The majority of studies on diffraction consider idealised situations with unidirectional, monochromatic waves propagating in deep water over a constant depth approaching an obstacle perpendicularly, mainly numerically or in wave tanks (Dalrymple and Kirby, 1988; Dalrymple et al., 1989; Monk et al., 2013, for instance); see also discussions in Yu et al. (2000). In the field, measuring diffraction is a cumbersome exercise. The spatial scales are several tens or hundreds of wavelengths along and across the propagation direction, which requires a dense network of point measurements to provide a detailed quantification. Such *in situ* measurements are clearly cost and operationally prohibitive. Altimeters on-board of satellites, nevertheless, can yield a broad picture along ground tracks (Andréfouët et al., 2012). However, the radar signal is corrupted in coastal regions — up to approximately 50 km from the coastline — and traditionally disregarded (Ribal and Young, 2019), exactly where diffraction effects are more remarkable. In recent years, a number of alternative algorithms have been proposed to improve coastal data quality also in terms of significant wave height (Schlembach et al., 2020). Among these, the Adaptive Leading Edge Subwaveform (ALES) algorithm has been applied to a wide range of altimetry missions and the reprocessed altimetry data are available to the scientific community (Passaro et al., 2014).

Synthetic Aperture Radar (SAR) is another potential source of wave measurements from satellites in regions where diffraction is significant. Depending on the operation mode, a SAR image can cover tens of kilometres in both azimuth and range directions, with resolution of the order of tens of meters. The most recent SAR satellite missions — such as TerraSAR-X and TanDEM-X, COSMO-SkyMed constellation, Radarsat-2 and Sentinel-1a — provide images with fine spatial resolution of the order of one meter (Lehner et al., 2012; Freeman et al., 2019). Li et al. (2010) employed sub-images around islands to derive a detailed picture of the wave spectral transformations. However, using image spectra rather than computing the directional wave spectrum, the authors did not discuss the variation of wave height. They focused on transformations in propagation direction and wavelength — which are readily extracted from image spectra — in the lee of a relatively small island. Wave spectra retrieval schemes are more prone to inaccuracies in low energy regions (Santos et al., 2021), exactly what is expected in the lee of an obstacle.

Here we analyse ALES reprocessed altimeter data in the vicinity of the Channel Islands off the coast of Southern California. The persistent presence of long swells reaching the islands all year round make them an interesting area for the investigation of wave transformations around obstacles. The remainder of the paper is organised as follows. A brief introduction of the theoretical background is discussed in Section 2. A description of the retracked altimeter data, the study area, the directional buoys and the numerical model appears in Section 3. Results are presented in Section 4 while general conclusions are presented in the Summary.

## 2. Theoretical background

### 2.1. Diffraction of water waves

The classical problem of diffraction of polarised light passing the edge of a screen was solved by the end of the 19th century (Sommerfeld, 1896). In the middle of the 20th century, Penny and Price (1952) provided an analytical solution considering diffraction of long crested linear water waves around the tip of an impermeable barrier. Following Penny and Price (1952), Boccotti (2000), McCormick and Kraemer (2002) and Kim et al. (2011) the behaviour of waves in the presence of a semi-infinite breakwater is briefly discussed (see Appendix A).

The general solution in the case of normal incidence of the waves on the breakwater is

$$F(x,y)=\frac{1+i}{2}\left(\mathrm{e}^{-iky}\int_{-\infty}^{\nu}\mathrm{e}^{-i(\pi/2)u^2}\,du+C_r\mathrm{e}^{iky}\int_{-\infty}^{\nu'}\mathrm{e}^{-i(\pi/2)u^2}\,du\right), \tag{1}$$

where $F(x,y)$ is a smooth function and $k$ is the wave number. Additionally, $\nu^2=\frac{4}{\lambda}(r-y)$, $(\nu')^2=\frac{4}{\lambda}(r+y)$, $\lambda=\frac{2\pi}{k}$, $r=\sqrt{x^2+y^2}$ and $C_r$ is the

reflection coefficient at the breakwater. For an oblique incidence of the waves on the breakwater, using polar coordinates ($x = r\cos\theta$ and $y = r\sin\theta$) we have

$$F(r,\theta) = \frac{1+i}{2}\left(e^{-ikr\sin\theta}\int_{-\infty}^{\nu} e^{-i(\pi/2)u^2}\,du + C_r e^{iksin\theta}\int_{-\infty}^{\nu'} e^{-i(\pi/2)u^2}\,du\right), \quad (2)$$

where $\nu^2 = \frac{4r}{\lambda}(1-sin\theta)$, $(\nu')^2 = \frac{4r}{\lambda}(1+sin\theta)$, $\lambda = \frac{2\pi}{k}$, $r = \sqrt{x^2+y^2}$ and $C_r$ is the reflection coefficient at the breakwater.

The solution presented in Penny and Price (1952) — Eqs. (1) and (2) — is for monochromatic wave diffraction on water of constant depth. Refraction and diffraction were treated separately for many years until theories combining these effects were proposed. An extension of the wave equation — originally for constant depth — was derived employing the assumption of slow variation of depth contours — the Mild Slope Equation, see main expressions in Appendix B.

The spacial rate of directional turn is given by

$$\frac{\partial\theta}{\partial s} = \frac{1}{\kappa}\frac{\partial\kappa}{\partial m} + \frac{1}{2(1+\delta_a)}\frac{\partial\delta_a}{\partial_m}. \quad (3)$$

where $s$ and $m$ are orthogonal axes, $m$ is in the direction of an iso-phase line and $s$ points in the direction of the displacement — these axes are used to describe the directional turning of an isophase line.

The spectral energy balance equation — disregarding the source terms — reads

$$\frac{\partial E}{\partial t} + \nabla\cdot\left((c_x, c_y, c_\theta)E\right) = 0, \quad (4)$$

where $E(\omega,\theta)$ is the wave energy density as function of $\omega$ and direction $\theta$, yielding

$$c_\theta = \frac{c_g}{k}\frac{\partial k}{\partial m} \quad (5)$$

and

$$C_\theta = C_g\left(\frac{1}{\kappa}\frac{\partial\kappa}{\partial m} + \frac{1}{2(1+\delta_a)}\frac{\partial\delta_a}{\partial_m}\right) \quad (6)$$

In Holthuijsen et al. (2003) the amplitude in the diffraction parameter $\delta_a$ was replaced by the normalised derivatives of the square root of the energy density, $\sqrt{E} = \sqrt{E(\Omega,\theta)}$ — where Ω is the intrinsic frequency — giving a new diffraction parameter

$$\delta_E = \frac{\nabla\cdot\left(cc_g\nabla\sqrt{E}\right)}{\kappa^2 cc_g\sqrt{E}}. \quad (7)$$

The expressions for diffraction-correct group velocity and directional turning rate Eq. (6), with the new diffraction parameter Eq. (7), were implemented in the SWAN model (Booij et al., 1999) to estimate the effect of bending direction. These diffraction corrections were derived neglecting the presence of currents, see discussion in Liau et al. (2011). Therefore, results in the vicinity of strong current gradients may be questionable. Additionally, the diffraction option should not be used when coherent reflection is expected, for instance in the vicinity of harbours with standing waves due to a phase coupling between the incident and reflected waves (Violante-Carvalho et al., 2009). In Ilic et al. (2007), the transformation of frequency and directional spectra around emerged breakwaters was assessed against laboratory and *in situ* data using SWAN with the diffraction option enabled. The authors reported the improvement of the prediction of wave height, particularly for broader directional distributions, with excellent agreement between model and measurements. The diffraction corrections in SWAN can be used in most oceanic conditions and, in particular, around emerged obstacles such as islands, with computational results in reasonable agreement with *in situ* and experimental data, as thoroughly reported in Holthuijsen et al. (2003).

### 2.2. Significant wave height from reprocessed satellite altimetry

A detailed description of the Adaptive Leading Edge Subwaveform — ALES — retracking process can be found in Passaro et al. (2014) and a validation exercise for $H_s$ in Passaro et al. (2015). Here, for completeness, the most relevant aspects for our analysis are outlined. Despite the relatively simple concepts embedded, satellite altimetry has substantially improved our understanding of the wave climate (Young, 1999) and ocean wave physics and prediction (Kalantzi et al., 2009; Gommenginger et al., 2019). A radar emits a short pulse of radiation that interacts with the sea surface within a footprint — the area covered by the radiation depends on the distance from the earth and the shape and size of the beam. Part of the incident radiation is backscattered to the sensor and the recorded waveforms are well described in the open ocean by a theoretical shape. The latter is, in the case of Jason-2 as well as the other standard altimetry missions (different from the latest Delay-Doppler altimeters), the so-called Brown functional form (Brown, 1977). This is characterised by a steep leading edge, whose steepness vary with significant wave height ($H_s$), and a slowly decaying trailing edge. The retrieval of geophysical parameters in satellite altimetry is based on the minimization of the differences between such a functional form and the real signal, in a process called retracking. In particular, $H_s$ is estimated from the slope of the leading edge of the altimetry waveform (Robinson, 2004).

In the coastal zone, the backscatter characteristics of the area illuminated by the satellite footprint are often inhomogeneous. Land that intrudes in the satellite footprint or patches of calmer waters caused for example by sheltered areas, show up in the trailing edge of the altimeter waveforms as power excess — the so-called bright targets. Bright targets cause the waveforms to deviate from the theoretical model and, therefore, hinder the retracking (Gomez-Enri et al., 2010). Retracking errors due to the presence of bright targets happen mostly up to 20 km from the coastline (Passaro et al., 2014), although they are also present in the open ocean (Queffeulou, 2004). Therefore, data in the coastal zone are routinely discarded and considered unreliable in standard products.

To solve this problem, the ALES retracker focuses on fitting the leading edge portion of the waveform, in order to avoid, as much as possible, the coastal contamination. In particular, it tunes the selection of the subwaveform to a first estimate of the sea state, to guarantee that coastal and open ocean noise performances are in line with classic *open ocean only* approaches (Passaro et al., 2014). Fig. 1 shows a typical ALES fitting of two altimetry waveforms in the open ocean (left) and in the coastal zone (right). In the right panel, a bright target is seen in the trailing edge. The ALES fitting is not affected, since the portion of the waveform considered does not include most of the trailing edge. The accuracy of altimeter measurements is usually determined through comparisons between models and *in situ* data — see for example Abdalla et al. (2010). A detailed discussion about the accuracy of the ALES retracked $H_s$ compared with wave buoys in the German Bight is presented in Passaro et al. (2015).

## 3. Data and methods

### 3.1. Retracked altimeter data

Satellite Altimetry waveforms distributed at 20 Hz (one measurement every 300 m along a satellite track) from the Jason-2 missions have been reprocessed using the ALES algorithm. Since the estimates at 20-Hz are strongly affected by noise, 1-Hz averages are computed, meaning a value of $H_s$ every 7 km along the track. Every latitude-longitude location provides, therefore, an averaged estimate of $H_s$ referred to an along-track dimension spanning 3.5 km before and after it. The across-track dimension of an altimetry estimates can be referred to the diameter of the circular area corresponding to the leading edge of the waveform, which for Jason-2 is about 2 km for a $H_s$ of 2 m (Yang et al., 2011).

According to Passaro et al. (2015), ALES improved the overall

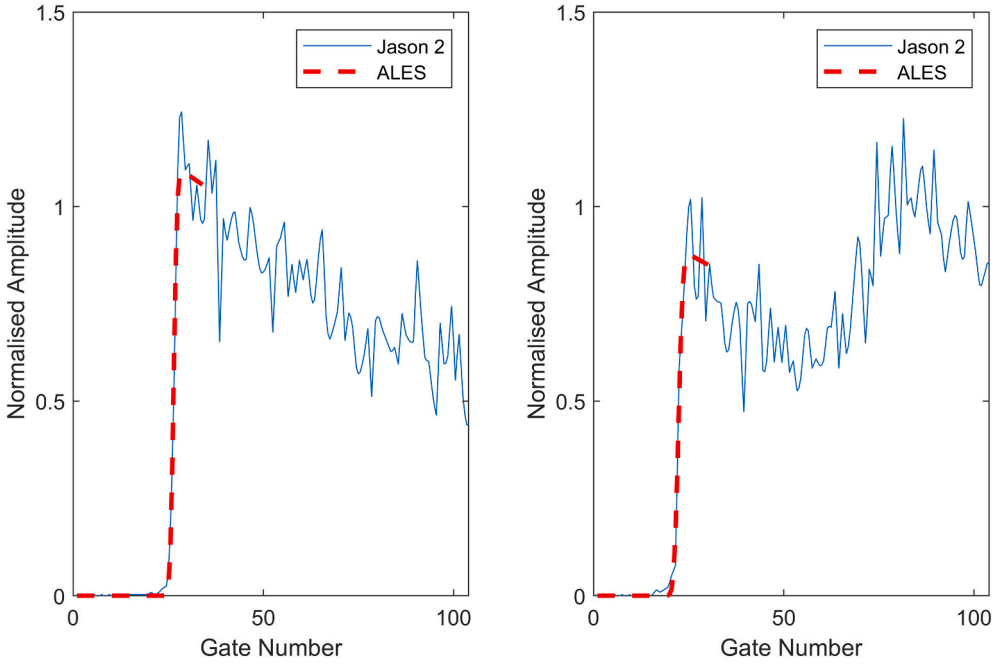


**Fig. 1.** Examples of ALES fitting (red) of two altimetry waveforms from Jason-2 at 20-Hz. In the open ocean (left, on 24-Jan-2009 11:13:30′ at 32.7°*S* and 119.3°*W*) and in the coastal zone (right, on 24-Jan-2009 11:13:20′ at 32.2°*S* and 119.5°*W*). (For interpretation of the references to colour in this figure legend, the reader is referred to the web version of this article.)

comparison of $H_s$ against buoys with respect to the original Jason-2 Geophysical Data Records with clear spatial improvements, particularly within distances of less than 20 km from the coastline. More specifically for this study, which considers 1-Hz averages, better results were obtained for one to three points towards the coast for each of the analysed tracks, meaning about 7 to 22 km of spatial improvement. Moreover, no systematic bias was reported. The analysis was restricted to conditions with $H_s < 2.5$ m, which are particularly challenging for the retrieval process due to the increased steepness of the leading edge and the consequent insufficient sampling (Smith and Scharroo, 2015). Values of $H_s$ retrieved from ALES were also used to successfully correct sea level estimations by means of the sea state bias correction, allowing higher precision (Passaro et al., 2018). While sea level data from ALES have been exploited in several coastal studies, the use of $H_s$ coastal estimations has not been considered yet and one of the objectives of this study is to combine this improved dataset with model and *in situ* data.

In the present work, Jason-2 significant wave height data retracked by ALES are employed spanning the period from 2008 to 2015, with 1-Hz averages which means an along track resolution of approximately 7 km. Jason-2 has one repeat cycle of 254 passes, revisiting the same ground-track within a margin of ±1 km every 9.9 days.

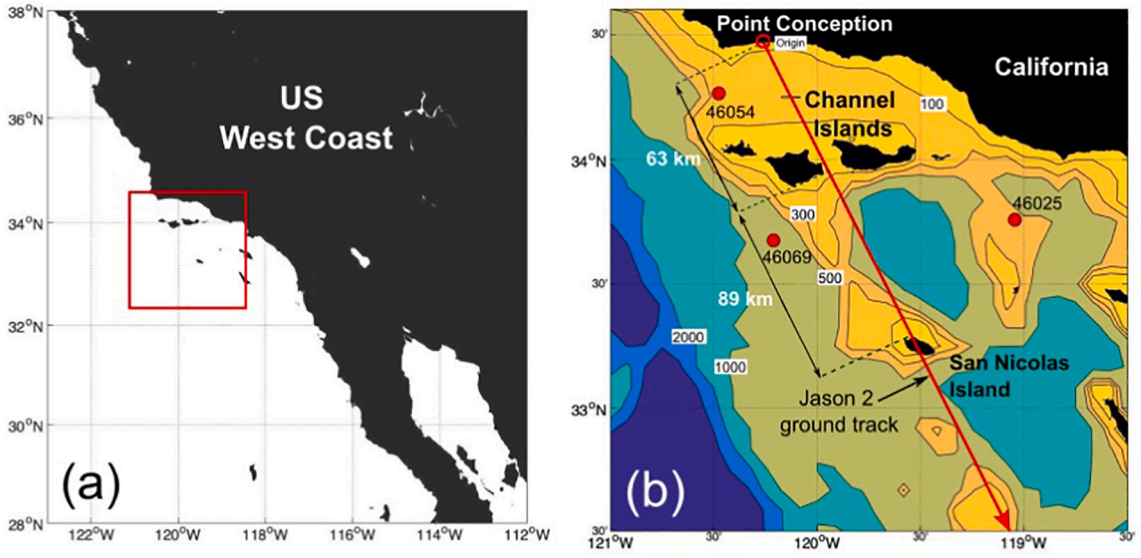


**Fig. 2.** The Channel Islands, Southern California, zoom out (a). In (b), the bathymetry of the area depicted as the red square in (a). Also shown the position of the two offshore directional buoys (46,054 and 46,069) and the onshore directional buoy (46,025). The red line is the segment of Jason-2 ground track used in the study. The distances between Point Conception, the Channel Islands and San Nicolas Island along the ground track are also shown. (For interpretation of the references to colour in this figure legend, the reader is referred to the web version of this article.)

### 3.2. Diffraction around the archipelago

The Channel Islands (Fig. 2) are a chain of islands off the coast of Southern California along the Santa Barbara Channel. The archipelago is exposed to swells from the Northern and Southern Hemispheres all year round, with the most energetic and longer ones coming from the northern quadrant (Adams et al., 2008; Crosby et al., 2019). There are several National Data Buoy Center (NDBC) buoys moored in the vicinity of the islands (O'Reilly et al., 2016), particularly three directional instruments — Stations 46,025, 46,054 and 46,069 in water depths respectively of 890 m, 454 m and 977 m (see their positions also in Fig. 2). The main archipelago encompasses a distance of approximately 100 km in the east-west orientation. The gaps between the islands are very shallow with most wave energy dissipated by breaking with no significant propagation through them. As an additional important feature, the depth around the islands varies sharply within short distances, reducing the relative importance of refraction.

Fig. 2 also depicts a Jason-2 ground track segment — pass number 206 with descending (north to south) ground track azimuth at the equator equal to 159.9° — which crosses the Channel Islands (34 ° *N* and 120 ° *W*) and a small island (San Nicolas, 33.25 ° *N* and 119.50 ° *W*). Naturally, the chosen ground track should be as aligned as possible with the selected direction of swell propagation. We are particularly interested in the long, more energetic, northerly swell, that impacts the region most of the year and whose direction is more aligned with the Jason-2 ground track that crosses the Channel Islands — Fig. 2. For the northerly waves, the orientation of the coast in Point Conception (34.50 ° *N* and 120.50 ° *W*) blocks most of the energy that could diffract around the easternmost tip of the archipelago (Adams et al., 2008). We are hence approximating the archipelago as a single shore-connected obstacle, with dimensions three orders of magnitude larger than the wavelengths of the incoming waves. Therefore diffraction is assumed to occur only around the westernmost tip of the archipelago, with no energy diffracted from the easternmost tip.

The NDBC directional buoys are employed to select wave spectra with the most energetic peak at least twice the energy level of the secondary peak — here designated as quasi-unimodal cases. They are also used to extract wave peak period, wave length, group velocity and direction and wind speed and direction. Directional spreading was computed as described in Rogers and Wang (2007). Additionally, only waves from the northwest quadrant are considered, approximately aligned with the satellite azimuth direction.

We have analysed all the available data from 2008 to 2015, with no restrictions on the magnitude of $H_s$, so that 41 events met these restrictive criteria. Fig. 3(a) depicts Jason-2 significant wave height between Point Conception and the Channel Islands (left part of the plot, between 0 and 60 km), between the Channel Islands and the island San Nicolas (60 km and 150 km) and after the island (150 km and 200 km). The distance runs from north to south along the ground track southward to Point Conception. The analysis focus on the ground track segment just southward to the archipelago up to the point just before the small island — 60 km to 150 km in Fig. 3(a). This segment is long enough for the energy of the propagating waves to reach an asymptote. The diffraction analysis is hence restricted to this ground track segment. The other two ground track segments are either too short — from Point Conception to the Channel Islands between 0 and 60 km — or the island is too small compared to the incident wavelengths — segment southward from island San Nicolas between 150 km and 200 km in Fig. 3(a).

In the lee of the archipelago $H_s$ increases nonlinearly and gradually reaches an assymptote value, the black thick line in Fig. 3(a) shows the average. In Fig. 3(b), to illustrate one of the 41 cases, we fit the profile

$$y = y_0 + b\tanh\frac{(x - x_0)}{L}, \tag{8}$$

where $x_0$ is the first point after the island, $y_0$ is $H_s$ at this point, $L$ is an e-folding scale and $b$ is the $H_s$ difference. The horizontal dotted line is the asymptotic (or limit) value for $H_s$, denoted $H_{s-lim}$. The along track distance, where $H_s$ reaches its limit value (in Eq. (8) the parameter $L$), is defined as the recovery distance.

In order to assess the quality of the cross validations between model or altimeter ($x$) against buoy data ($y$), four statistical parameters are employed: Bias, root-mean square error (RMSE), scatter index (SI) and Pearson correlation coefficient (corr), that is

$$Bias = \frac{1}{n}\sum_{i=1}^{n}(x_i - y_i), \tag{9}$$

$$RMSE = \sqrt{\frac{1}{n}\sum_{i=1}^{n}(x_i - y_i)^2}, \tag{10}$$

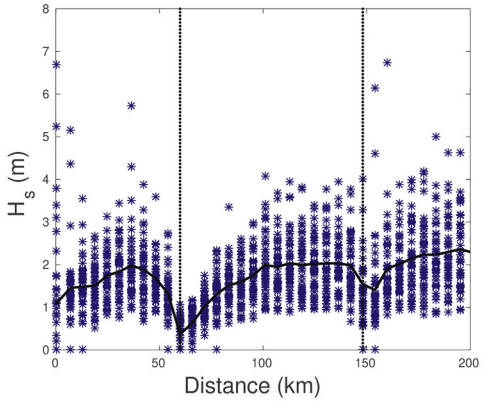


(a) $H_s$ along the ground track shown in Figure 2 for the 41 selected cases.

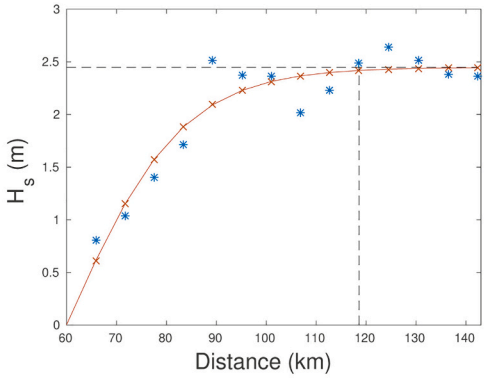


(b) Values of *recovery distance* and $H_{s-lim}$ to reach the asymptote.

**Fig. 3.** Significant wave height $H_s$ measured with Jason-2 along a segment of ground track number 206. Data spans the period from 2008 to 2015, with quasi-unimodal spectra selected with direction of propagation from the NW quadrant, yielding 41 cases. In (a), distance runs from north to south, zero is the northmost point in the vicinity of where the ground track crosses the continent — see Fig. 2. Therefore the northwesterly waves are propagating from the left of the plot to the right of the plot. The leftmost vertical bar represents the position of the Channel Islands, the rightmost one the small island San Nicolas. Black thick line is the mean $H_s$. In (b), example of one of the 41 selected cases shown in (a) for the ground track segment in between the two vertical lines. The asterisks are the altimeter data and the full red line is data fit using Eq. (8). The asymptote is computed and the values of *recovery distance* and where $H_s$ reaches its limit value ($H_{s-lim}$) are determined for each case. (For interpretation of the references to colour in this figure legend, the reader is referred to the web version of this article.)

$$SI = \frac{\sqrt{\frac{1}{n}\sum_{i=1}^{n}(x_i - y_i)^2}}{\frac{1}{n}\sum_{i=1}^{n} y_i}, \tag{11}$$

$$corr = \frac{cov(x,y)}{\sigma_x \cdot \sigma_y}, \tag{12}$$

where $n$ is the number of observations, cov(x,y) represents the covariance between the two variables and ($\sigma_x$, $\sigma_y$) are the standard deviations.

### 3.3. Numerical model description

The SWAN cycle III version 41.31 phase-averaged model was used to investigate the wave pattern in the lee of the Channel Islands, where diffraction effects are expected to be significant. The model solves the action density balance equation in time, geographical and spectral space — the governing equations are thoroughly discussed in Booij et al. (1999). The directional space was computed with 10° resolution — 36 directions — and 31 frequencies ranging from a minimum frequency of 0.04 Hz to a maximum frequency of 1 Hz. The model was run in stationary mode because of the relatively short residence time of the waves in the geographical domain (Fig. 4(a)).

SWAN was mainly employed to gain a better understanding of the relative importance of the various processes. More importantly, a phase resolving model — for instance a Boussinesq model or a model based on the MSE — would not allow an evaluation of the relative (separate) importance of diffraction and refraction, which in SWAN can easily be activated or de-activated individually.

Unless otherwise stated (when specific tests were proposed), the runs were performed on the default set-up of the model — the quadruplet wave-wave interactions and source/sink terms were de-activated and diffraction was activated. Diffraction is a non-default option implemented from version 40.41 onwards (see details in Holthuijsen et al., 2003, and in Section 2). Our strategy for mitigating numerical diffusion in geographic space is to use high resolution *via* unstructured grids (Rogers et al., 2002; Kim et al., 2017). A high resolution unstructured grid was built using SMS (Surface-Water Modeling System) for automatic mesh generation with a longitude range from 119°W to 121°W and a latitude range from 32.5°N to 34.5°N (Fig. 4(a)) — the ETOPO1 bathymetry was downloaded from www.ngdc.noaa.gov. The grid is composed of 78,161 vertices and 146,376 cells, with minimum grid size of 17.8 m and maximum of 10,401 m, with resolution increasing in regions where diffraction effects are important. The output wave parameters discussed in the paper were required on this grid, with no interpolations performed. Additionally, the same wave parameters were estimated over grid points coincident with Jason-2 ground track.

Directional wave spectra from the NDBC buoys simultaneous with Jason-2 data — time difference of less than 30 min — were used as input at the boundaries. The offshore buoys (46,054 and 46,069, see Fig. 2) were employed on the North and West side of the computational grid, respectively, or on both sides in the absence of one of the spectra. Moreover, the onshore buoy 46,025 was used on the South side of the grid. The 41 cases shown in Fig. 3(a), whose peak wave directions and 1D spectra were available for the selection process, were initially considered for the simulations with the numerical model. However, for the year 2009 and for both offshore buoys, the spectral wave direction data — archive alpha2 in the NDBC data base — were missing and therefore 10 spectra were not computed and hence not used as input for SWAN simulations. Consequently, there are 31 coincident cases employed in the numerical simulations — one of them is depicted in Fig. 4(b).

## 4. Results and discussion

### 4.1. Energy recovery along the direction of propagation

In nature, diffraction rarely occurs disassociated from other shallow water wave phenomena such as shoaling, reflection, breaking and — mainly — refraction. The wave propagation speed depends on depth and when the crests approach shallow water at an oblique angle they tend to gradually become parallel to the bottom contours. The factor to determine whether the accumulated change in direction is significant is the ratio of the horizontal gradient of depth variation to the incident wavelength. The modulation in wave direction due to changes in the bathymetry in coastal areas, in general, is relevant since water depth slowly varies increasing the relative importance of refraction in respect with the other shallow water phenomena. The assumption of mild slopes is key for the formulation of propagation and transformation theories considering the combined effect of refraction and diffraction (Radder, 1979; Madsen and Sørensen, 1992).

The supposition of mild slopes does not hold in the present case — see Fig. 4(a). The depth is greater than 300 m only 10 km away from the archipelago, in both up and down-wave directions. In the vicinity of its westernmost tip, the depth sharply drops from 100 m to 0 in about 5 km. As waves move into shallow water, their propagation is affected when they reach depths of about half their wavelength. A wave with length of

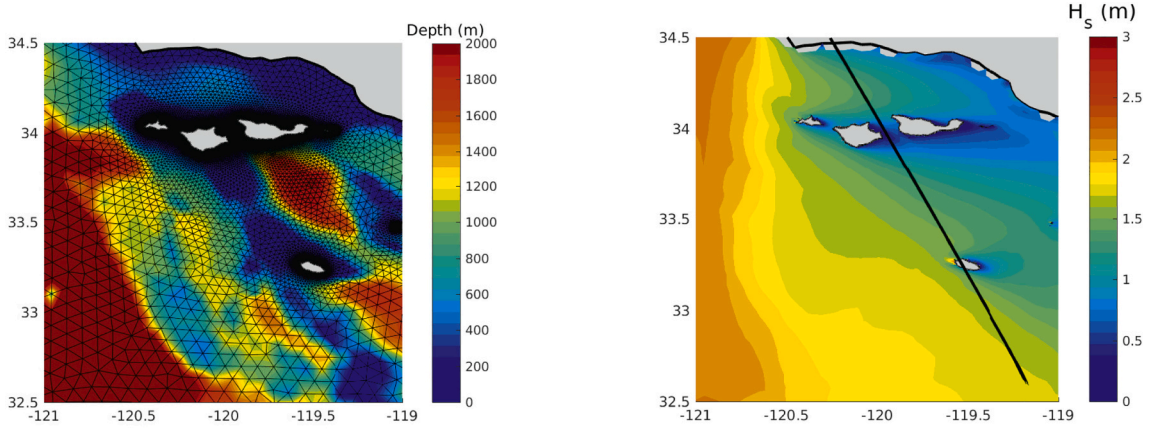


(a) Computational area and grid. (b) $H_s$ spatial distribution.

**Fig. 4.** SWAN computational area and the unstructured grid — colors represent water depth (a). In (b), one of the 31 coincident cases with peak wave direction $\theta = 311^\circ$ for April 4$^{th}$ 2015 at 05:00) showing the Channel Islands as an effective obstacle to the wave propagation — $H_s$ down-wave is nearly zero in the vicinity of the archipelago. Jason-2 ground track depicted as the thick black line and the colors represent $H_s$.

200 m will hence propagate 5 km — roughly 25 wavelengths — when refraction commences and, less than that, for effective changes in direction to be discernible. That is a relatively short distance and therefore the importance of refraction with respect to diffraction is expected to be small.

An example of the spatial distribution of peak wave direction computed by SWAN is shown in Fig. 5(a), in addition to $H_s$ — for a peak wave direction $\theta = 311^\circ$ measured by the buoy which spectrum was employed as offshore boundary input for the simulation (the whole computational domain is depicted in Fig. 4(b)). The shadow effect of the archipelago as a single obstacle is clear, with down-wave $H_s$ in the vicinity of the islands nearly zero gradually increasing further away —

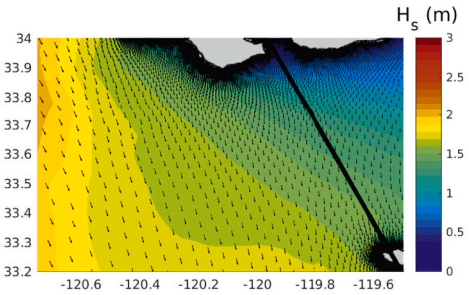


(a) One of the 31 coincident cases to illustrate the pattern of peak wave direction estimated by the numerical model.

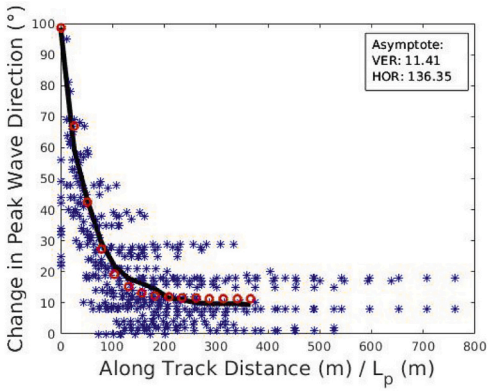


(b) Rate of change of wave direction along the normalised ground track — run R1.

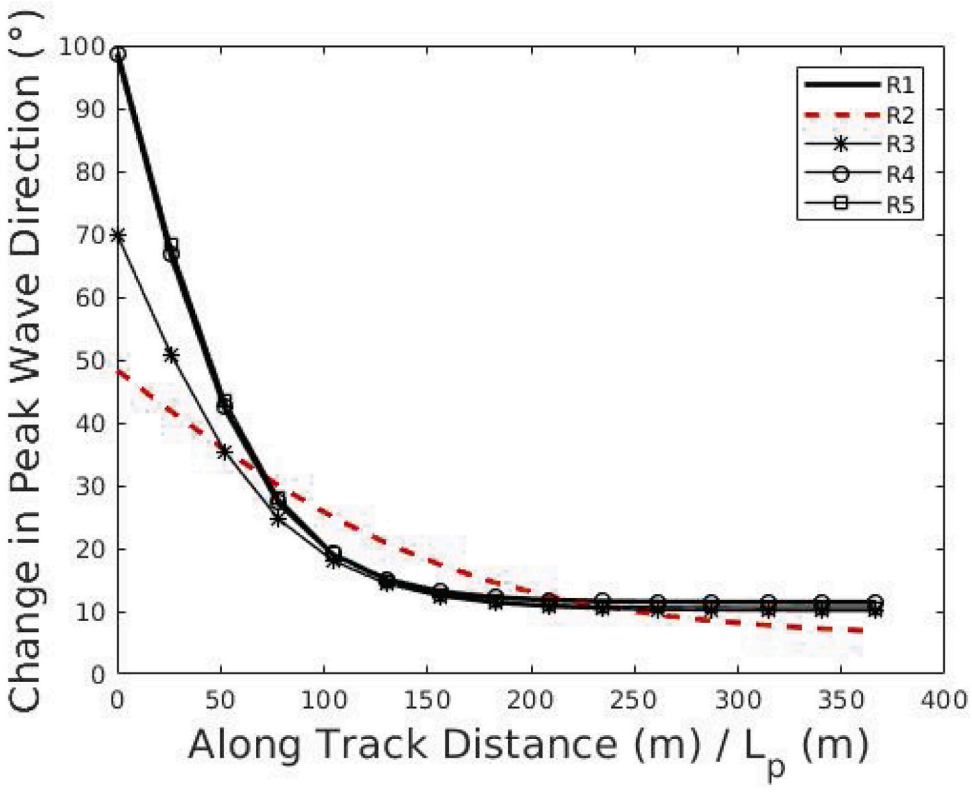


(c) Rate of change of wave direction along the normalised ground track for the five distinct SWAN runs.

**Fig. 5.** In (a), zoom in down-wave the archipelago of the same case shown in Fig. 4(b). The colour bar indicates $H_s$ and the thick black line is Jason-2 ground track — the arrows indicate peak wave direction, their lengths are proportional to the magnitude of $H_s$. In (b), the horizontal axis is the ratio between the along track distance in the lee of the archipelago — segment shown in (a) — and the peak wavelength $L_p$ measured by the offshore buoy. The asterisks are the absolute difference between the offshore buoy peak wave direction and the peak wave direction over the normalised ground track estimated by the numerical model. Therefore the vertical axis is the change of peak wave direction with respect to the incident peak wave direction. The thick black line is the mean value of the 31 coincident cases for run R1 — see Table 1 — and the red circles depict its fit using Eq. (8). The values of the asymptote are also displayed. The five simulations listed in Table 1 are shown in (c) depicting the fit of the mean value of the 31 coincident cases for every run using Eq. (8). (For interpretation of the references to colour in this figure legend, the reader is referred to the web version of this article.)

also shown in Fig. 3(a) and (b). Energy migrates from the westernmost tip towards the shadow zone, as expected, with no energy coming from the easternmost tip. The Jason-2 ground track is also shown in Fig. 4(b), crossing the Channel Islands and around 90 km down-wave also crossing San Nicolas Island. The following analysis is focused on this ground track segment.

The relative change in peak wave direction along the normalised ground track estimated by the numerical model is depicted in Fig. 5(b) and (c). Five different model configurations are listed in Table 1 with model options activated or de-activated (R1–R4) and an additional run with very high spectral resolution (R5). In Fig. 5(b), the simulations were performed with both processes of diffraction and refraction activated; whitecapping, depth-induced breaking and nonlinear quadruplet wave interactions de-activated — spectral resolution of 36 directions and 31 frequencies. This is the standard configuration (R1) for our simulations. SWAN default configuration settings were applied to the remaining parameters, as previously discussed. The run R1 configuration was applied to the simulations shown in Fig. 4(b) and all others, unless otherwise stated. The thick black line in Fig. 5(b) is the mean rate of change of direction for the 31 coincident cases — its fit is also shown using Eq. (8) with the vertical and horizontal asymptotes (see Table 1 and Fig. 5(c) as well). On average — for run R1 — the waves propagate 136.3 wavelengths before reaching the limit direction, with a 11.4° deviation from the peak propagation direction measured at the offshore buoy. The simulation was repeated with the same configuration but de-activating the process of diffraction whereas refraction was kept activated — run R2 — and on average the waves have to propagate 338.5 wavelengths (more than twice the number of wavelengths in run R1) to attain the limit peak direction. The rate of change in direction, compared to run R1, is significantly more slow when diffraction is not enabled. Moreover, considering the opposite configuration (diffraction activated and refraction de-activated — run R3) the number of wavelengths to attain the limit peak wave direction is similar to run R1. The model directional resolution is 10°, therefore the three simulations attain a similar down-wave direction within the numerical resolution. Simulations R1-R3 confirm the importance of diffraction over refraction in the vicinity of the Channel Islands.

Runs R1 and R4 are identical and therefore whitecapping, depth-induced breaking and nonlinear quadruplet wave interactions are of less importance in our simulations. Numerical diffusion is an artefact that appears due to the discretization process during propagation, hence becoming smaller at higher — spectral and geographical — resolutions. Diffusion in spectral space is investigated by testing with high spectral resolution — sensitivity test. With a much finer spectral (frequency/directional) discretization — 72 bins in directional space and 45 in frequency ranging from a minimum of 0.04 Hz to a maximum of 1 Hz — run R5 is also nearly identical to run R1. Numerical diffusion in spectral space is found to be small — the refined spectral resolution in run R5 does not impact the overall results.

Fig. 6 shows the diffraction coefficient — ratio between down-wave and incident $H_s$ — *versus* normalised along track distance, measured by the altimeter (Fig. 6(a)) and estimated by the numerical model (Fig. 6 (b)). Both plots depict the gradual energy increase in the lee of the archipelago up to a limit value. The 31 coincident cases encompass values of offshore buoy steepness $\varepsilon = \frac{H_s \pi}{L_p}$ (where $L_p$ is the peak wavelength) ranging from 0.01 to 0.05, peak wave direction $\theta$ varying from 285° to 324°, peak period $T_p$ from 8.3 s to 17.4 s and directional spreading $\sigma$ from 16° to 51°. The average wind speed measured at the onshore buoy is 6.7 $ms^{-1}$ and mean direction is 287°. Despite the more scattered values of the altimeter, on average both plots are similar with reasonable agreement between the numerical model and measured values. The incoming wave energy is reduced in the lee of the archipelago due to wave breaking and reflection, and the reduction is more pronounced in the SWAN simulations. On average, the diffracted $H_s$ measured by the altimeter reaches a limit around 300 wavelengths and is reduced by 16%. The simulated diffracted $H_s$ with SWAN reaches its limit value earlier — 250 wavelengths — and is more severely attenuated — 29%.

Considering regular waves, Penny and Price (1952) demonstrated that an exact solution can be obtained for a fully reflecting, semi-infinite thin and impermeable obstacle on water of constant depth. Furthermore, the amount of reflected energy affects the diffracted energy in the shadow zone. SWAN does not accurately represent reflection and diffraction simultaneously (Violante-Carvalho et al., 2009), with poor convergence during the iteration process in stationary runs. In the present simulations, the archipelago is considered as a fully absorbing obstacle, hence there is no reflected energy. This dependence is expected to be reduced in cases of irregular waves with a certain amount of directional spreading using the phase-decoupled approximation included in SWAN. Even so, the model clearly underestimates the limit value of energy. To tune the model parameters for processes such as reflection from obstacles, bottom friction or depth-induced breaking — to name a few — is beyond our scope in this work, with its default configuration being used (see SWAN user manual for details).

The overall behaviour observed in Fig. 6 can be more thoroughly examined taking into account other spectral parameters extracted from the offshore buoys. The comparisons between incident $H_s$ and the limit values $H_{s-lim}$ from Jason-2 and SWAN (respectively $H_{s-limJ}$ and $H_{s-limS}$) considering all cases are shown in Fig. 7, plotted together with the computed directional spreading from the offshore buoys — respectively Fig. 7(a) and (c). The agreement between altimeter and buoy data is better than model and buoy, with smaller values of RMSE, Bias and SI. The model estimates that $H_{s-limS}$ is more attenuated than the altimeter measurements — as already discussed in Fig. 6. The effects of incident wave heights and wind speed measured at the onshore buoy on the ratio $\frac{H_{s-limJ}}{H_s}$ have also been examined and are insignificant.

In Ilic et al. (2007), directional wave spectra were obtained in shallow water in the vicinity of one of the gaps of six shore-parallel, emerged breakwaters using several pressure transducers and surface-piercing wave staffs. The authors reported that down-wave dissipation is frequency dependent, with shorter waves more attenuated than longer, low frequency waves. Such dependency was not observed in our data. The energy reduction in the lee of the archipelago has no obvious relation with the offshore buoy peak period. The dependence on offshore buoy steepness, on the other hand, is noticeable though still not large. The average ratio $\frac{H_{s-limJ}}{H_s}$ is 0.86 for $\varepsilon \geq 0.025$ and is slightly reduced to 0.83 for $\varepsilon < 0.025$. The cut-off value 0.025 is roughly the median used to split the number of measurements in half to assure statistical confidence. In the following, the same approach is applied to the remaining

**Table 1**
SWAN configuration for five distinct runs: Refraction (REF), Diffraction (DIF), Whitecapping (WCAP), Depth-induced breaking (BREAK), Nonlinear quadruplet wave interactions (QUAD), Number of directions (#DIR) and Number of frequencies (#FREQ). In addition VER and HOR are, respectively, the vertical and horizontal asymptotes computed from Eq. (8).

| Run | REF | DIF | WCAP | BREAK | QUAD | #DIR | #FREQ | VER | HOR |
|---|---|---|---|---|---|---|---|---|---|
| R1 | ON | ON | OFF | OFF | OFF | 36 | 31 | 11.4 | 136.3 |
| R2 | ON | OFF | OFF | OFF | OFF | 36 | 31 | 5.7 | 338.5 |
| R3 | OFF | ON | OFF | OFF | OFF | 36 | 31 | 10.0 | 158.1 |
| R4 | ON | ON | ON | ON | ON | 36 | 31 | 11.4 | 136.3 |
| R5 | ON | ON | OFF | OFF | OFF | 72 | 45 | 10.6 | 140.3 |

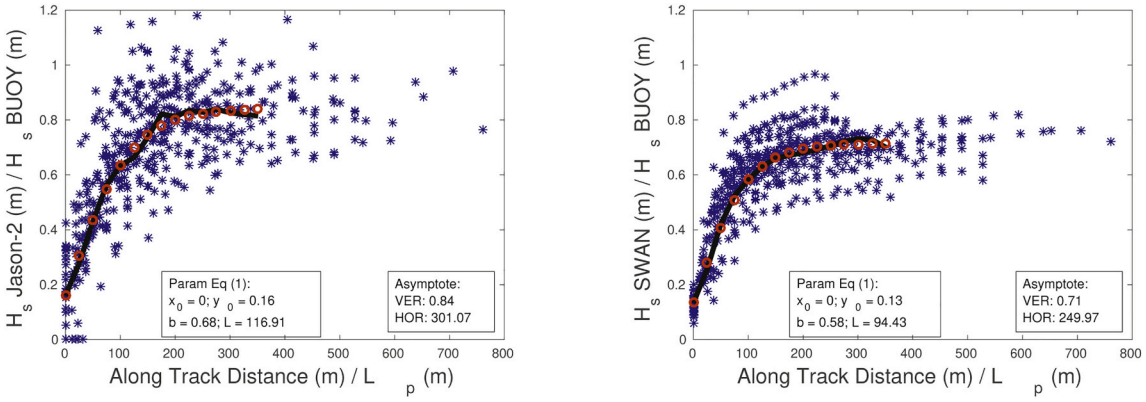


(a) Jason-2. (b) SWAN.

**Fig. 6.** The diffraction coefficient as a function of non-dimensional distance. The horizontal axis is the ratio between the along track distance in the lee of the archipelago and the peak wavelength $L_p$ measured by the offshore buoy. The vertical axis is the ratio between the diffracted $H_s$ measured by Jason-2 (a) or estimated by the numerical model (b) and the incident $H_s$ measured by the same offshore buoy. The thick black line is the mean of the 31 coincident cases. The red circles depict the fit using Eq. (8). The values of the asymptote are also displayed (lower right corner panel) and the parameters of Eq. (8) (lower central panel). (For interpretation of the references to colour in this figure legend, the reader is referred to the web version of this article.)

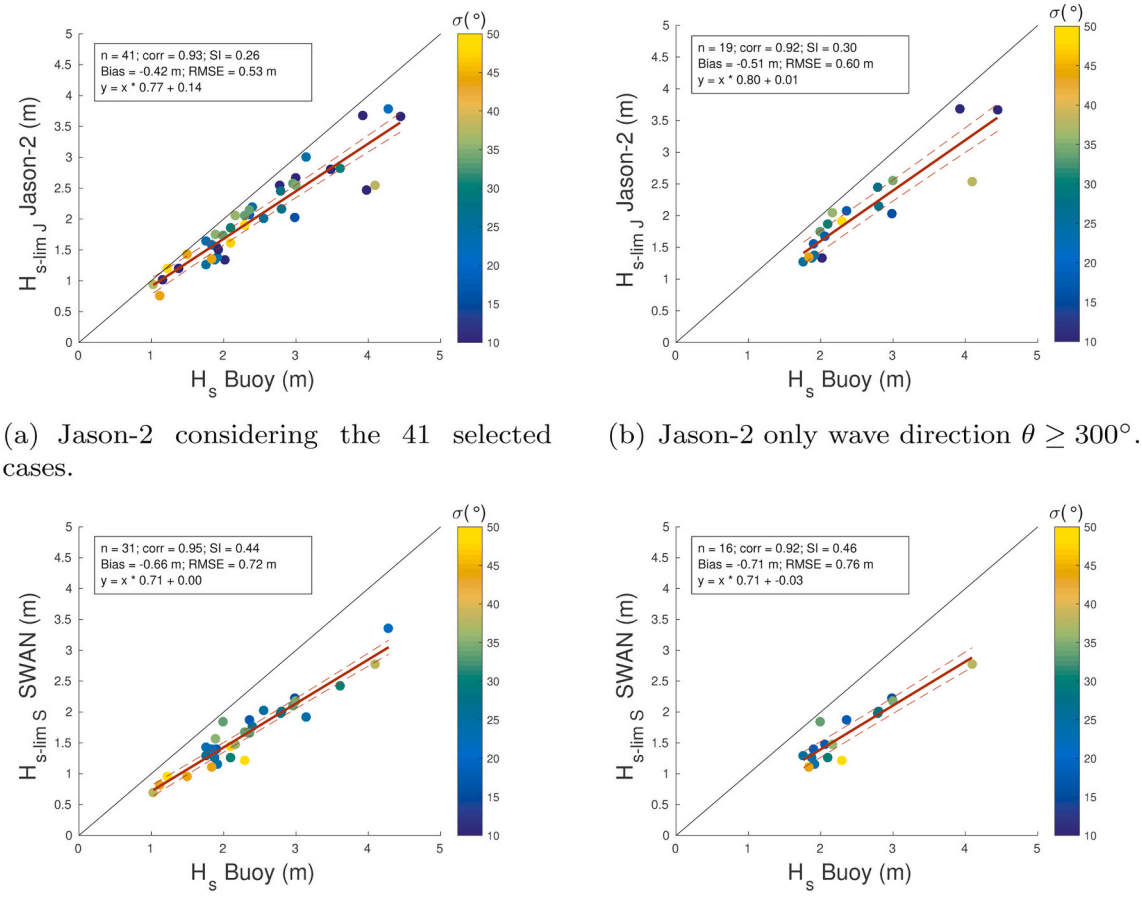


(a) Jason-2 considering the 41 selected cases. (b) Jason-2 only wave direction $\theta \geq 300°$.

(c) SWAN considering the 31 coincident cases. (d) SWAN only wave direction $\theta \geq 300°$.

**Fig. 7.** Incident $H_s$ measured by one of the directional offshore buoys (46,054 or preferentially 46,069, whenever there is available directional data) against the limit value $H_{s-lim}$ in the lee of the archipelago — computed as presented in Fig. 3(b). The colorbar is the offshore buoy directional spreading $\sigma$. The 45° full line is the perfect fit and the red full line is the least-squares fit — dashed lines indicate the 95% confidence intervals. In (a) all cases measured by Jason-2 (denominated as $H_{s-limJ}$) are displayed with wave propagation direction $\theta$ varying from 285° to 324°, in (b) only those with $\theta \geq 300°$. Also shown the number of observations ($n$), the Pearson Correlation Coefficient (corr), Bias, root mean square error (RMSE) and the least-squares fit equation. In (c,d), same as (a,b) for the limit value in the lee of the archipelago estimated by SWAN — $H_{s-limS}$. (For interpretation of the references to colour in this figure legend, the reader is referred to the web version of this article.)

parameters measured by the offshore buoys.

A numerical investigation about the effects of directional spreading on an array of wave energy converters considered as a series of permeable breakwater segments was presented in Monk et al. (2013). The waves were simulated only for a normal incidence angle relative to the array and the reduction in wave height on its lee side along a central transect was discussed. The final energy reduction, a number of wavelengths down-wave, was larger for very narrow directional spreading, compared to broader spreading, confirming other published results in wave tanks (for example, Briggs et al., 1995; Yu et al., 2000). Here, the buoy directional spreading has a small effect on $\frac{H_{s-limJ}}{H_s}$. For broader spreading, with $\sigma \geq 30°$, the average ratio is 0.86. The waves are slightly more attenuated for narrow directional spreading — $\sigma < 30°$ — with the average ratio reduced to 0.83. The incident offshore wave peak directions are not constant for a given range of directional spreadings in our altimeter dataset — as usually is imposed in numerical experiments or wave tanks. Hence, the determination of the relative importance of directional spreading over incidence angle is not clear when considering the whole range of incident offshore directions — $\theta$ varying from 285° to 324°.

In Figs. 7(a) and 7(c) all available data are displayed, spanning the whole range of incident offshore propagation directions. Considering only the events more collinear with the along track direction ($\theta \geq 300°$ in Fig. 7(b) and (d)) the values of RMSE, Bias and SI of the subsampled ensemble are larger, indicating more discrepancy between $H_s$ and $H_{s-lim}$ and hence larger wave energy attenuation. There is, therefore, a more clear relationship between wave attenuation and incident offshore wave peak direction. The average ratio $\frac{H_{s-limJ}}{H_s}$ is 0.80 for $\theta \geq 300°$ with $\overline{\sigma} = 30°$ (where the overbar represents average) while it is 0.88 for $\theta < 300°$ with $\overline{\sigma} = 32°$. At $\theta < 300°$ more energy is directed from the west and hence gets behind the islands. Considering all selected cases, $\theta$ varies from 285° to 324°. Hence, the range of incident directions for $\theta \geq 300°$ in Fig. 7(b) equals 24° for an average directional spreading of 30°. Therefore, the range of offshore incident peak wave directions is smaller than the average value of the directional spreading. The incident offshore peak wave direction is more effective in determining the amount of energy in the lee of the islands rather than the directional spreading *per se*, within the narrow range of directions from the NW window considered. Energy can propagate down-wave by diffraction and advection as well, which implies that changes in the peak wave direction by a couple tens of degrees does affect the energy recovery pattern more significantly than the width of the directional spreading.

Although $H_{s-limJ}$ did not show an obvious relationship with the steepness measured by the offshore buoy, the recovery distance, on the other hand, is clearly dependent on $\varepsilon$. Fig. 8 depicts the offshore buoy steepness $\varepsilon$ against the number of wavelengths necessary to reach the limit value — ratio between recovery distance and peak wavelength $L_p$. Less steep waves, with higher peak periods, propagate less wavelengths to attain the energy limit. The model performance is reasonably good when compared with altimeter data, describing the same overall behaviour. SWAN estimates that $H_{s-limS}$ is reached in a smaller number of wavelengths (Fig. 8(b)) in comparison with Jason-2 data (Fig. 8(a)). Moreover, similar to Fig. 7(b) and (d), selection of propagation directions more aligned with Jason-2 ground track ($\theta \geq 300°$, not shown in the plots) can alter the results. Waves propagating over this range of directions are more attenuated, so that the number of wavelengths to reach $H_{s-limJ}$ increases — the expression shown in Fig. 8(a) becomes $y = x * 9260.33 - 18.35$ — highlighting the main role played by the incident peak wave direction in comparison with the directional spreading. The number of wavelengths to reach the limit value has no obvious dependence on $\sigma$, on the ratio $\frac{H_{s-limJ}}{H_s}$, nor on the wind speed measured at the onshore buoy.

### 4.2. Energy reduction across the direction of propagation

In principle, because of the finitude of wave crests, diffraction is one of the attenuation processes acting on swell as they propagate away from a storm area. In the open ocean the lateral gradients in crest height will be small and hence diffraction is expected to be also small but not negligible. Its relative importance among the other phenomena responsible for wave energy attenuation is not clear, mainly because of the inherent complexity of measurements over many tens or hundreds of wavelengths, both along and across its propagation direction. Global models do not compute diffraction and in some of them it appears as a non-default option generally activated only around emerged obstacles or in shallow water with complex bathymetry. Hence, diffraction is currently not included as an attenuation process during propagation in numerical models.

An attempt to quantify the rate of lateral diffraction of monochromatic waves in a tank of 10 m width, 50 m long and 5 m deep was presented by Babanin and Waseda (2015). In their experiments, mechanically generated crests shorter than the tank's width, with distinct steepnesses, were monitored around 50 wavelengths. As expected, as the waves crossed the tank, energy decreased gradually as it was spread to the initially flat surface. They concluded that the rate of lateral energy migration to the undisturbed region — $\nu$ in $ms^{-1}$ — is a function of wave

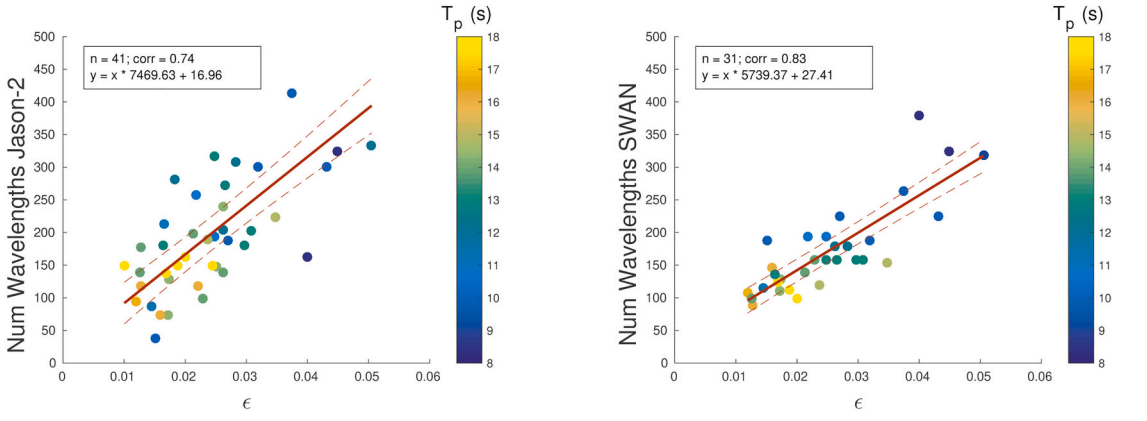


(a) Considering the 41 selected cases. (b) Considering the 31 coincident cases.

**Fig. 8.** Offshore buoy steepness $\varepsilon = \frac{H_s \pi}{L_p}$ against the number of wavelengths to reach the limit — ratio between the down-wave recovery distance (as shown in Fig. 3 (b)) and the offshore buoy peak wavelength $L_p$. In (a) Jason-2, in (b) SWAN. The red full line is the least-squares fit and the dashed lines indicate the 95% confidence intervals — equation shown on top of both plots. The colorbar is the offshore buoy peak period $T_p$. (For interpretation of the references to colour in this figure legend, the reader is referred to the web version of this article.)

steepness and group velocity. Another set of experiments combined crests half the tank's width with concomitant waves, with same amplitude and period but phase shifted of 180° and occupying the other half of the tank, with the same crest length to avoid a flat surface. The lateral spreading of energy and therefore diffraction was interrupted, with no significant energy reduction as previously observed.

The rate of lateral diffraction — orthogonally to the propagation direction — is computed using our altimeter and model data. Given an offshore peak wave direction, a diffraction separation line is drawn tangential to the westernmost tip of the archipelago — blue line in Fig. 9 illustrating, as an example, a peak wave direction $\theta = 324°$. After hitting the archipelago, the diffraction separation line is the boundary between the area where the waves are not affected by the islands and the shadow, sheltered area. The computed recovery distance ($D_{REC}$) along the ground track, as illustrated in Fig. 3(b), is also shown for this example. An orthogonal segment to the diffraction separation line is computed passing through $D_{REC}$, yielding the distance of lateral diffraction ($D_{LD}$) — dashed line in Fig. 9. Additionally, the distance from the westernmost tip of the archipelago up to the projection of $D_{REC}$ on the diffraction separation line is denominated as $D_{PD}$. Based on the peak group velocity $C_g$ measured at the offshore buoy, the time of wave propagation along $D_{PD}$ is determined — $T_{PD} = \frac{D_{PD}}{C_g}$ (in $s$). The rate of lateral diffraction ($\nu_d$ in $ms^{-1}$) is defined as the ratio between the distance of lateral diffraction and the estimated time of wave propagation along the diffraction separation line ($\nu_d = \frac{D_{LD}}{T_{PD}}$). Energy migrates down-wave laterally increasing its value gradually along the ground track up to the limit position ($D_{REC}$). Therefore $\nu_d$ is an estimate of the rate of lateral energy migration — spreading caused by diffraction — into the shadow area in the lee of the islands.

The recovery distance $D_{REC}$ is closely dependent on the offshore peak period — longer waves attain the limit value in less wavelengths than shorter ones (Fig. 8). In some occasions, depending on the peak period and the offshore peak wave direction, the diffraction separation line crosses the Jason-2 ground track before $D_{REC}$ and therefore a distance of lateral diffraction $D_{LD}$ cannot be estimated. Hence, for Jason-2, the distance of lateral diffraction was successively determined in 10 cases whereas SWAN yielded 13 cases — presented in Fig. 10.

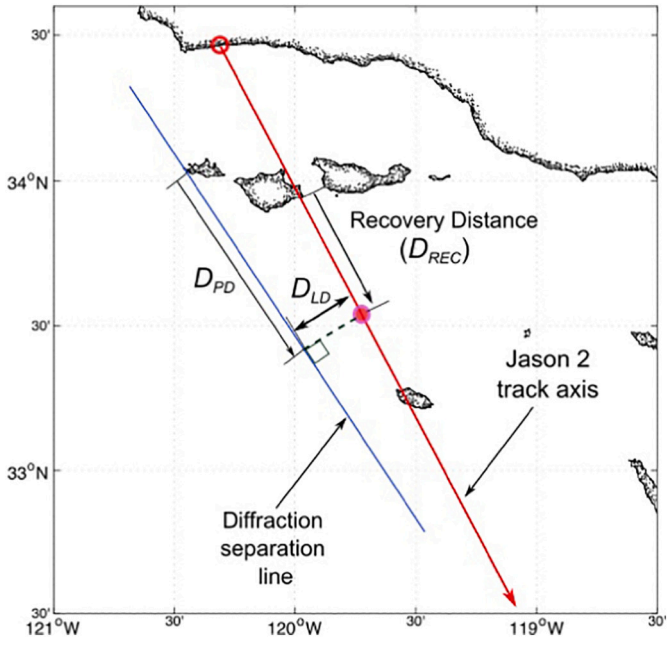


**Fig. 9.** The red line is the segment of Jason-2 ground track used in the study, whereas the blue line is a given peak wave direction at the offshore buoy — 324° in the example depicted — tangent to the westernmost tip of the archipelago and designated as diffraction separation line. $D_{REC}$ is the position of one of the computed recovery distances along the ground track — see Fig. 3(b). The orthogonal from $D_{REC}$ up to the diffraction separation line is the distance of lateral diffraction $D_{LD}$ — dashed line. Moreover, $D_{PD}$ is the distance from the westernmost tip of the archipelago up to the projection of $D_{REC}$ on the diffraction separation line. (For interpretation of the references to colour in this figure legend, the reader is referred to the web version of this article.)

Fig. 10(a) and (c) depict, respectively, the ratio between the rate of lateral diffraction — $\nu_{dJ}$ for Jason-2 and $\nu_{dS}$ for SWAN — and offshore group velocity $C_g$ against offshore wave steepness $\varepsilon$. The relationship for monochromatic waves mechanically generated in a tank proposed in Babanin and Waseda (2015), which corresponds to the direction of normal incidence, is also shown — dashed line. To investigate the influence of the directional spreading and steepness on the rate of lateral diffraction, SWAN test case simulations were performed using as forcing JONSWAP spectra with an incident peak wave direction of 300°. Nine simulations with different values of peak wave steepness were run for a fixed value of directional spreading $\sigma = 10°$ and then repeated for $\sigma = 20°$. The ratio $\frac{\nu_d}{C_g}$ was accordingly estimated for the test case simulations — represented by full lines blue and red, respectively, in Fig. 10(a) and (c). For monochromatic waves, Babanin and Waseda (2015) pointed out that in the limit $\varepsilon \to 0$ the value $\frac{\nu_d}{C_g} \to 0.1$, the asymptote to the theoretical linear solution for a finite breakwater (Penny and Price, 1952) — their wave tank data reached a smaller value of 0.08. For broader waves, SWAN simulations indicate that the limit value of $\frac{\nu_d}{C_g}$ increases when $\varepsilon \to 0$ — to approximately 0.10 for $\sigma = 10°$ and approximately 0.18 for $\sigma = 20°$. The ratio $\frac{\nu_d}{C_g}$, derived from SWAN test simulations and measured in the wave tank, decreases as the waves become more unidirectional, that is with smaller spread. The altimeter data in Fig. 10(a) indicate this dependence, with larger values of $\frac{\nu_{dJ}}{C_g}$ for larger values of $\sigma$ — the same is not clearly observed in Fig. 10(c) for $\frac{\nu_{dS}}{C_g}$. The dependence of $\frac{\nu_{dJ}}{C_g}$ and $\frac{\nu_{dS}}{C_g}$ on wind speed and $H_s$ measured at the onshore buoy is marginal, as well as $T_p$, $\theta$ and $H_s$ at the offshore buoy. However, the dependence of $\nu_{dJ}$ on $\sigma$ is clear — Fig. 10(b) — for broader waves, the rate of lateral diffraction is faster. The same is not observed, however, in the model results (Fig. 10 (d)), with no dependence of $\nu_{dS}$ on $\sigma$.

It is also clear with the curves shown in Fig. 10(a) and (c), derived from SWAN test case simulations and measured in the wave tank, that the ratio $\frac{\nu_d}{C_g}$ increases gradually with steepness. That is not evident from the altimeter data or the SWAN runs using as input the offshore buoy spectra. The values of $\frac{\nu_{dJ}}{C_g}$ and $\frac{\nu_{dS}}{C_g}$ *versus* $\varepsilon$ in Fig. 10(a) and (c) have similar behaviours and both peak respectively at $\varepsilon = 0.023$ and $\varepsilon = 0.030$, decreasing for larger and smaller values of steepness. The scatter observed in Fig. 10(a) of $\frac{\nu_{dJ}}{C_g}$ around the curves of the SWAN test case simulations and the wave tank relationship is not surprising and is, probably, related to the broad range of incident peak wave directions and directional spreadings. In contrast, the curves are given by relationships of unidirectional and monochromatic waves in a tank and also of irregular waves with fixed values of spreading and propagation direction for the test case simulations. Nevertheless, the values of $\frac{\nu_{dJ}}{C_g}$ in Fig. 10(a) for irregular waves propagating with distinct directions and spreadings have the same order of magnitude of the theoretically calculated for monochromatic waves (Penny and Price, 1952), simulated with SWAN and measured in a wave tank, which increases our confidence on the altimeter data results.

Our data differ from Babanin and Waseda (2015) in many aspects. We are considering irregular waves much less steep than those monochromatic and mechanically generated in a tank. The range of incident peak wave directions and directional spreadings clearly affects the diffraction patterns, overcoming the dependence on steepness and group velocity that they found. However, the mean values of $\frac{\nu_{dJ}}{C_g}$ and $\frac{\nu_{dS}}{C_g}$ are, respectively, 0.20 and 0.13 — within the range of ratios reported in Babanin and Waseda (2015).

Here we are considering a very particular situation in oceanic con-

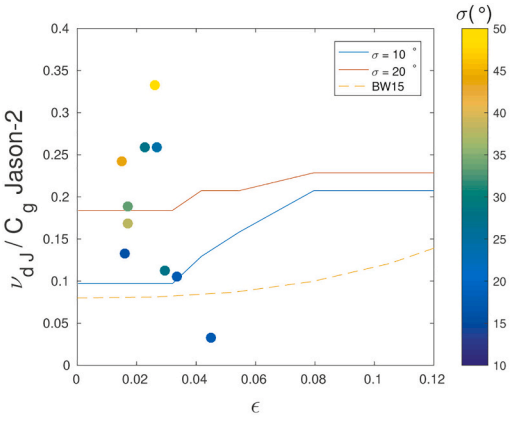


(a) $\nu_{dJ}$ was determined in 10 cases.

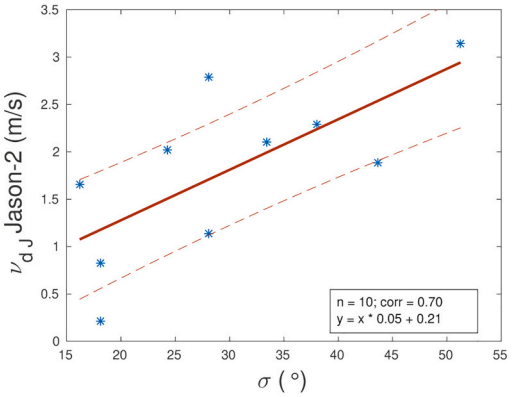


(b) Dependence of $\nu_{dJ}$ on spreading.

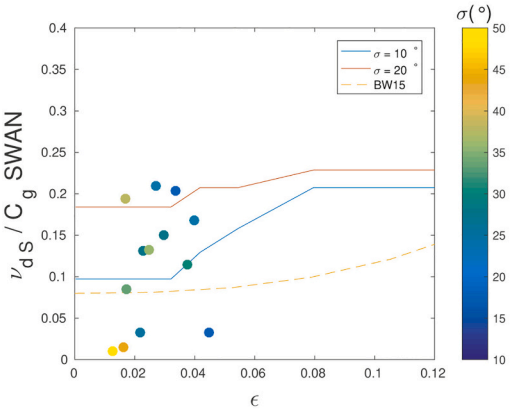


(c) $\nu_{dS}$ was determined in 13 cases.

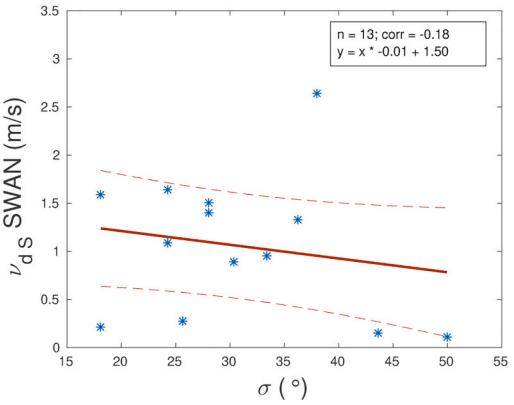


(d) Dependence of $\nu_{dS}$ on spreading.

**Fig. 10.** Offshore buoy steepness $\varepsilon = \frac{H_s \pi}{L_p}$ against the ratio between the rate of lateral diffraction along swell crests ($\nu_d$, $ms^{-1}$) and group velocity estimated from the offshore buoy ($C_g$, $ms^{-1}$) for Jason-2 (a) and SWAN (c). The colorbar is the offshore buoy directional spreading $\sigma$. The dashed line is the relationship for monochromatic waves proposed in Babanin and Waseda (2015) whereas the full lines are the test case simulations with SWAN for JONSWAP spectra with $\sigma = 10Kd$ and $\sigma = 20°$. The relationship between the offshore buoy directional spreading and the rate of lateral diffraction along swell crests, respectively for Jason-2 and SWAN, is shown in (b) and (d). The red full line is the least-squares fit and the dashed lines indicate the 95% confidence intervals — equation, correlation coefficient and number of points shown on plots. (For interpretation of the references to colour in this figure legend, the reader is referred to the web version of this article.)

ditions. Energy is totally blocked by the archipelago and diffraction down-wave is responsible for its lateral spreading, rapidly occupying an area where a strong gradient along crest was present. However, the ratio $\frac{\nu_{dJ}}{C_g}$ is quite high. If such a rate of lateral diffraction was acting during propagation in ordinary situations, caused by the finite length of wave crests as they move away from the storm areas, then waves would attenuate unrealistically quick. A possible explanation was suggested based on the wave tank data (Babanin and Waseda, 2015). Whenever the energy gradient along crest caused by diffraction occurred simultaneously with background wave energy, the lateral spreading was severely interrupted.

The occurrence of such gradients in crest height on otherwise undisturbed sea surfaces seem to be rare in the ocean even in the low wind conditions of the equatorial zone — monthly climatologies of $H_s$ were presented for instance in Young (1999). Considering 37 years of spectral data from the European Centre for Medium-Range Weather Forecasts — employing the ECWAM model — Portilla-Yandún et al. (2016) proposed a methodology for wave spectra partitioning and long-term statistics. A global climatology is available in the GLOSWAC data base, presenting a probability distribution of wave spectral partitions. Multi-modal spectra in the Atlantic, Pacific and Indian Equatorial Oceans — not shown here — is the normal situation year-round. Even during events with very low wind speeds, the occurrence of a single swell component seems to be improbable, as normally there are at least two. The total lack of background energy during swell propagation therefore appears to be rare but not impossible and that would result in very rapid wave amplitude reduction over short distances, which has not been reported to date.

## 5. Summary

Our analysis combines a novel dataset of retracked altimeter measurements, directional buoy data and numerical model estimates to investigate the effects of diffraction. This approach was applied to the vicinity of the Channel Islands, where the greater importance of diffraction with respect to refraction means it is an ideal area to study the complex changes occurring in the lee of an emerged obstacle. Considering quasi-unimodal waves roughly aligned with a Jason-2 ground track segment, energy transformations along and across the wave propagation direction were investigated for a variety of incident offshore directions, steepnesses, directional spreadings, peak periods and energies. We believe that this is the first reported measurements of diffraction of irregular waves in the ocean over a relative large number of wavelengths — data typically greater than 300 wavelengths.

In the lee of the archipelago, along the propagation direction, energy increases with the number of propagated wavelengths and gradually reaches a limit. This behaviour is well described by Eq. (8) and, on

average, the energy limit is reached after 300 wavelengths for the altimeter data. The numerical simulations described a similar behaviour but $H_s$ was more severely reduced in a smaller number of wavelengths. The limit value presented a stronger dependence on the incident peak wave direction rather than on the width of the directional spreading — the dependence on wind speed, incident peak period, steepness and $H_s$ were marginal. The other parameter of relevance is the distance along the ground track necessary to attain the limit, which is strongly dependent on steepness. Less steep waves require fewer wavelengths to attain an asymptotic value of $H_s$.

The lateral rate of energy spreading across the wave propagation direction ($\nu_d$) is computed, for the first time in oceanic conditions. The ratios $\frac{\nu_d}{C_g}$ from altimeter and SWAN simulations are of the same magnitude as those reported in a wave tank experiment. Moreover, a direct dependence of $\frac{\nu_d}{C_g}$ on directional spreading is observed with the altimeter data. Despite the eight years of retracked altimeter data employed, the restrictive selection criteria reduced significantly the amount of data available for our analysis. An increase in the dataset, to gain statistical robustness, might be achieved employing a substantially larger period of coincident measurements between altimeter and buoy. Additionally, phase resolving models could be used, with a high computational burden, to possibly corroborate the preliminary findings described in Fig. 10(a) and (b) — which is beyond the scope of the present work.

Diffraction is associated with strong energy gradients, expected to occur down-wave of emerged obstacles or when finite crest length swells are crossing a region with lack of background energy. While emerged obstacles obviously occur frequently, the absence of other spectral components during propagation seems to be a rare event, even in regions well known for low wind speed values. Diffraction is one of the non-dissipative processes acting during propagation and the reported values of $\frac{\nu_d}{C_g}$ might have implications in numerical simulations under the conditions here discussed.

## Declaration of Competing Interest

None.

## Acknowledgment

NVC would like to acknowledge the very helpful discussions with Dr. Ian Young and Dr. Gerbrant van Vledder on an early version of the manuscript.

## Appendix A

Considering Cartesian coordinates with the origin being at the tip of the breakwater and the positive $x$-axis along the breakwater (Fig. 11). Depth is assumed as constant with $z = -d$ at the bottom and $z = 0$ at the still water surface. The water plane is defined by $x$ and $y$ and the $z$-axis is upward orthogonal to this plane. For incompressible fluid and irrotational flow, there is a velocity potential, $\phi(x,y,z,t)$, whose Laplacian is equal to zero.

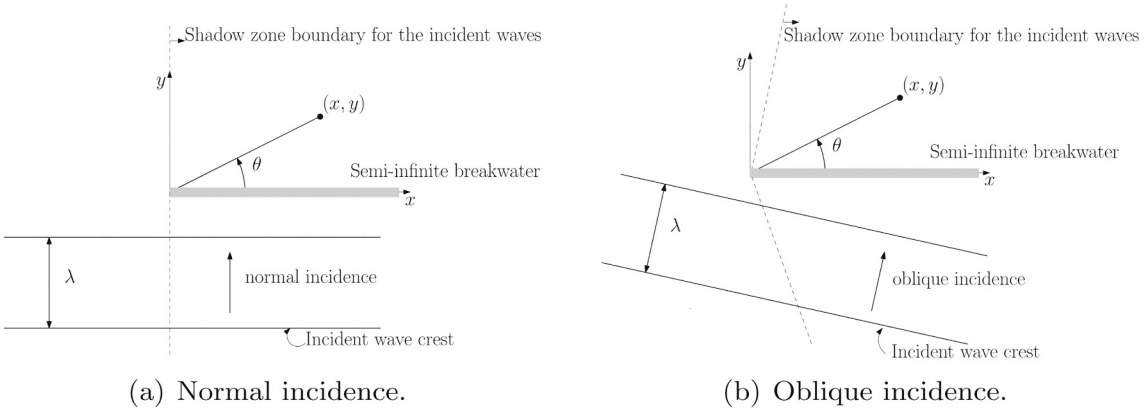


**Fig. 11.** Schematic diagram for waves approaching a breakwater: (a) normal and (b) oblique incidence.

The velocity potential can be represented by — considering the periodicity and the no-flow boundary condition at the bottom:

$$\phi(x,y,z,t) = A\cosh(k(z+d))F(x,y)e^{i\omega t}, \tag{13}$$

where $A$ is a constant — related to wave amplitude, angular frequency, wave number, gravity and water depth — $k$ is the wave number, $\omega$ is the angular frequency and with $F(x,y)$ a smooth function that has to obey the Helmholtz equation

$$\frac{\partial^2 F}{\partial x^2} + \frac{\partial^2 F}{\partial y^2} + k^2 F = 0 \tag{14}$$

which is a time independent form of the wave equation that describes the propagation of the wave motion in space and time. Applying boundary conditions, the solution for $F(x,y)$ in Eq. (2) is given by

$$F(x,y) = e^{-iky}F_1(x,y) + e^{iky}F_2(x,y) \tag{15}$$

## Appendix B

The so-called Mild Slope Equation (MSE), first presented in Berkhoff (1972), is given by (Holthuijsen et al., 2003; Ilic et al., 2007; Rusu et al., 2008)

$$\nabla\cdot\left(cc_g\nabla\xi\right)+\kappa^2cc_g\xi=0, \tag{16}$$

where $c=\frac{\omega}{\kappa}$, $\kappa$ is the separation parameter from $\omega^2=g\kappa\tanh(\kappa d)$, $g$ is the gravitational acceleration and $d$ is the water depth, $\omega$ is the radian frequency and $c_g=\frac{\partial\omega}{\partial\kappa}$. Let

$$\xi=aexp(i\psi) \tag{17}$$

be a complex wave function of a harmonic wave, where Re($\xi$ exp ($i\omega t$)) is the ocean surface elevation as a function of time, $a(x,y)$ is the stationary amplitude and $\psi(x,y)$ is the phase function.

Assuming $\omega$ constant and multiplying Eq. (1) by the complex conjugate of $\xi$, after removing its imaginary part we obtain

$$\nabla\left(\frac{k}{\kappa}c_ga^2\right)=0. \tag{18}$$

In the presence of diffraction the group velocity is

$$C_g=\frac{k}{\kappa}c_g, \tag{19}$$

and substituting Eq. (2) into (1) we obtain

$$k^2=\kappa^2+\frac{\nabla\cdot\left(cc_g\nabla a\right)}{cc_ga}. \tag{20}$$

The second term on the right-hand side represents diffraction in the phase function $\psi$. Denoting the diffraction parameter as

$$\delta_a=\frac{\nabla\cdot\left(cc_g\nabla a\right)}{\kappa^2cc_ga}, \tag{21}$$

the diffraction-correct phase velocity is

$$C=\frac{\omega}{k}=c(1+\delta_a)^{-1/2}, \tag{22}$$

with the diffraction-correct group velocity

$$C_g=c_g(1+\delta_a)^{1/2}. \tag{23}$$

## References


Abanades, J., Greaves, D., Iglesias, G., 2015. Coastal defence using wave farms: the role of farm-to-coast distance. Renew. Energy 75, 572–582.

Abdalla, S., Janssen, P., Bidlot, J., 2010. Jason2 OGDR wind and wave products: monitoring, validation and assimilation. Mar. Geodesy 33, 239–255.

Adams, P.N., Inman, D.L., Graham, N.E., 2008. Southern California deep-water wave climate: characterization and application to coastal processes. J. Coast. Res. 24 (4) pages 1022–1035.

Andréfouët, S., Ardhuin, F., Queffeulou, P., Gendre, R.L., 2012. Island shadow effects and the wave climate of the Western Tuamotu Archipelago (French Polynesia) inferred from altimetry and numerical model data. Mar. Pollut. Bull. 65 (10), 415–424.

Ardhuin, F., Chapron, B., Collard, F., 2009. Observation of swell dissipation across oceans. Geophys. Res. Lett. 36 (6).

Babanin, A.V., Waseda, T., 2015. Diffraction and instability of short-crested limited-length one-dimensional coherent wave trains. In: Proceedings of the 34 International Conference on Ocean, Offshore and Arctic Engineering pages 1–7.

Berkhoff, J., 1972. Computations of combined refraction, diffraction and reflection. In: Proceedings of the 13th International Conference on Coastal Engineering. ASCE, New York page 471–490.

Boccotti, P., 2000. Wave Mechanics for Ocean Engineering. Elsevier.

Booij, N., Ris, R.C., Holthuijsen, L.H., 1999. A third-generation wave model for coastal regions: 1. Model description and validation. J. Geophys. Res. Oceans 104 (C4), 7649–7666.

Briggs, M.J., Thompson, E.F., Vincent, C.L., 1995. Wave diffraction around breakwater. J. Waterw. Port Coast. Ocean Eng. 121 (1), 23–35.

Brown, G., 1977. The average impulse response of a rough surface and its applications. IEEE Trans. Antennas Propag. 25 (1), 67–74.

Collard, F., Ardhuin, F., Chapron, B., 2009. Monitoring and analysis of ocean swell fields from space: new methods for routine observations. J. Geophys. Res. Oceans 114 (C7).

Crosby, S.C., Kumar, N., O'Reilly, W.C., Guza, R.T., 2019. Regional swell transformation by backward ray tracing and SWAN. J. Atmos. Ocean. Technol. 36 (2), 217–229.

Dalrymple, R.A., Kirby, J.T., 1988. Models for very wide-angle water waves and wave diffraction. J. Fluid Mech. 192, 33–50.

Dalrymple, R.A., Suh, K.D., Kirby, J.T., Chae, J.W., 1989. Models for very wide-angle water waves and wave diffraction. Part 2. Irregular bathymetry. J. Fluid Mech. 201, 299–322.

de León, S., Guedes Soares, C., 2005. On the sheltering effect of islands in ocean wave models. J. Geophys. Res. Oceans 110 (C9).

Do, J.D., Jin, J.-Y., Hyun, S.K., Jeong, W.M., Chang, Y.S., 2020. Numerical investigation of the effect of wave diffraction on beach erosion/accretion at the Gangneung Harbor, Korea. J. Hydro Environ. Res. 29, 31–44.

Elshinnawy, A.I., Medina, R., González, M., 2018. On the influence of wave directional spreading on the equilibrium planform of embayed beaches. Coast. Eng. 133, 59–75.

Fang, K., Wang, H., Sun, J., Zhang, J., Liu, Z., 2019. Including wave diffraction in XBeach: model extension and validation. J. Coast. Res. 36 (1), 116–127.

Freeman, A., Zink, M., Caro, E., Moreira, A., Veilleux, L., Werner, M., 2019. The legacy of the SIR-C/X-SAR radar system: 25 years on. Remote Sens. Environ. 231, 111255.

Goda, Y., Takayama, T., Suzuki, T., 1978. Diffraction diagrams for directional random waves. In: Proceedings of 16th Conference on Coastal Engineering, Hamburg, Germany, 16 pages 628–650.

Gomez-Enri, J., Vignudelli, S., Quartly, G.D., Gommenginger, C.P., Cipollini, P., Challenor, P.G., Benveniste, J., 2010. Modeling envisat ra-2 waveforms in the coastal zone: case study of calm water contamination. IEEE Geosci. Remote Sens. Lett. 7 (3), 474–478.

Gommenginger, C., Chapron, B., et al., 2019. Seastar: a mission to study ocean submesoscale dynamics and small-scale atmosphere-ocean processes in coastal, shelf and polar seas. Front. Mar. Sci. 6, 457.

Hasselmann, K., 1962. On the non-linear energy transfer in a gravity-wave spectrum part 1. General theory. J. Fluid Mech. 12 (4), 481–500.

Holthuijsen, L., Herman, A., Booij, N., 2003. Phase-decoupled refraction–diffraction for spectral wave models. Coast. Eng. 49 (4), 291–305.

Ilic, S., van der Westhuysen, A., Roelvink, J., Chadwick, A., 2007. Multidirectional wave transformation around detached breakwaters. Coast. Eng. 54 (10), 775–789.

Janssen, T.T., Herbers, T.H.C., Battjes, J.A., 2008. Evolution of ocean wave statistics in shallow water: refraction and diffraction over seafloor topography. J. Geophys. Res. Oceans 113 (C3).

Jiang, H., Stopa, J.E., Wang, H., Husson, R., Mouche, A., Chapron, B., Chen, G., 2016. Tracking the attenuation and nonbreaking dissipation of swells using altimeters. J. Geophys. Res. Oceans 121 (2), 1446–1458.

Kalantzi, G.D., Gommenginger, C., Srokosz, M., 2009. Assessing the performance of the dissipation parameterizations in WAVEWATCH III using collocated altimetry data. J. Phys. Oceanogr. 39 (11), 2800–2819.
Kim, H., Do, K.D., Suh, K.-D., 2011. Scattering of obliquely incident water waves by partially reflecting non-transmitting breakwaters. Ocean Eng. 38 (1), 148–158.
Kim, G.H., Jho, M.H., Yoon, S.B., 2017. Improving the performance of SWAN modelling to simulate diffraction of waves behind structures. J. Coast. Res. 79 (sp1), 349–353.
Lehner, S., Pleskachevsky, A., Bruck, M., 2012. High-resolution satellite measurements of coastal wind field and sea state. Int. J. Remote Sens. 33 (23), 7337–7360.
Li, X., Lehner, S., Rosenthal, W., 2010. Investigation of ocean surface wave refraction using TerraSAR-X data. IEEE Trans. Geosci. Remote Sens. 48 (2), 830–840.
Liau, J.-M., Roland, A., Hsu, T.-W., Ou, S.-H., Li, Y.-T., 2011. Wave refraction–diffraction effect in the wind wave model WWM. Coast. Eng. 58 (5), 429–443.
Madsen, P.A., Sørensen, O.R., 1992. A new form of the Boussinesq equations with improved linear dispersion characteristics. Part 2. A slowly-varying bathymetry. Coast. Eng. 18 (3), 183–204.
McCormick, M.E., Kraemer, D.R., 2002. Polynomial approximations for Fresnel integrals in diffraction analysis. Coast. Eng. 44 (3), 261–266.
Mendes, D., Fortunato, A.B., Bertin, X., Martins, K., Lavaud, L., Silva, A.N., Pires-Silva, A. A., Coulombier, T., Pinto, J.P., 2020. Importance of infragravity waves in a wave-dominated inlet under storm conditions. Cont. Shelf Res. 192, 104026.
Monk, K., Zou, Q., Conley, D., 2013. An approximate solution for the wave energy shadow in the lee of an array of overtopping type wave energy converters. Coast. Eng. 73, 115–132.
O'Reilly, W., Olfe, C.B., Thomas, J., Seymour, R., Guza, R., 2016. The California coastal wave monitoring and prediction system. Coast. Eng. 116, 118–132.
Passaro, M., Cipollini, P., Vignudelli, S., Quartly, G.D., Snaith, H.M., 2014. ALES: a multi-mission adaptive subwaveform retracker for coastal and open ocean altimetry. Remote Sens. Environ. 145, 173–189.
Passaro, M., Fenoglio-Marc, L., Cipollini, P., 2015. Validation of significant wave height from improved satellite altimetry in the german bight. IEEE Trans. Geosci. Remote Sens. 53 (4), 2146–2156.
Passaro, M., Nadzir, Z.A., Quartly, G.D., 2018. Improving the precision of sea level data from satellite altimetry with high-frequency and regional sea state bias corrections. Remote Sens. Environ. 218, 245–254.
Penny, W., Price, A., 1952. Part I. The diffraction theory of sea waves and the shelter afforded by breakwaters. Philos. Trans. R. Soc. B 244, 236–253.
Peregrine, D.H., 1967. Long waves on a beach. J. Fluid Mech. 27 (4), 815–827.
Portilla-Yandún, J., Salazar, A., Cavaleri, L., 2016. Climate patterns derived from ocean wave spectra. Geophys. Res. Lett. 43 (22), 11,736–11,743.
Queffeulou, P., 2004. Long-term validation of wave height measurements from altimeters. Mar. Geod. 27 (3–4), 495–510.
Radder, A.C., 1979. On the parabolic equation method for water-wave propagation. J. Fluid Mech. 95 (1), 159–176.
Resio, D.T., 1987. Shallow-water waves. I: theory. J. Waterw. Port Coast. Ocean Eng. 113 (3), 264–281.
Resio, D.T., 1988. A steady-state wave model for coastal applications. In: 21st International Conference on Coastal Engineering pages 929–940.
Ribal, A., Young, I.R., 2019. 33 years of globally calibrated wave height and wind speed data based on altimeter observations. Sci. Data 77 (6), 501–511.
Robinson, I.S., 2004. Measuring the Oceans From Space: The Principles and Methods of Satellite Oceanography. Springer/Praxis Publishing.
Rogers, W.E., Wang, D.W.C., 2007. Directional validation of wave predictions. J. Atmos. Ocean. Technol. 24 (3), 504–520.
Rogers, W.E., Kaihatu, J.M., Petit, H.A.H., Booij, N., Holthuijsen, L.H., 2002. Diffusion reduction in an arbitrary scale third generation wind wave model. Ocean Eng. 29 (11), 1357–1390.
Rusu, E., Pilar, P., Guedes Soares, C., 2008. Evaluation of the wave conditions in Madeira archipelago with spectral models. Ocean Eng. 35 (13), 1357–1371.
Santos, F.M., Santos, A.L., Violante-Carvalho, N., Carvalho, L.M., Brasil-Correa, Y.O., Portilla-Yandun, J., Romeiser, R., 2021. A simulator of Synthetic Aperture Radar (SAR) image spectra: the applications on oceanswell waves. Int. J. Remote Sens. 42 (8), 2981–3001.
Schlembach, F., Passaro, M., Quartly, G.D., Kurekin, A., Nencioli, F., Dodet, G., Piollé, J.-F., Ardhuin, F., Bidlot, J., Schwatke, C., et al., 2020. Round robin assessment of radar altimeter low resolution mode and delay-doppler retracking algorithms for significant wave height. Remote Sens. 12 (8), 1254.
Smith, W.H.F., Scharroo, R., 2015. Waveform aliasing in satellite radar altimetry. IEEE Trans. Geosci. Remote Sens. 53 (4), 1671–1682.
Snodgrass, F.E., Groves, G.W., Hasselmann, K.F., Miller, G.R., Munk, W.H., Powers, W. H., 1966. Propagation of ocean swell across the pacific. Philos. Trans. R. Soc. Lond. 259 (1103), 431–497.
Sommerfeld, A., 1896. Mathematische theorie der diffraction. Math. Ann. 47 (2), 317–374.
Toledo, Y., Agnon, Y., 2009. Nonlinear refraction–diffraction of water waves: the complementary mild-slope equations. J. Fluid Mech. 641, 509–520.
Vincent, C.L., Briggs, M.J., 1989. Refraction-diffraction of irregular waves over a mound. J. Waterw. Port Coast. Ocean Eng. 115 (2), 269–284.
Violante-Carvalho, N., Paes-Leme, R.B., Accetta, D.A., Ostritz, F., 2009. Diffraction and reflection of irregular waves in a harbor employing a spectral model. Ann. Braz. Acad. Sci. 81, 837–848.
Wiegel, R.L., 1962. Diffraction of waves by semi-infinite breakwater. J. Hydraul. Div. 88 (1), 27–44.
Yang, L., Sen Lin, M., Zhang, Y., Bao, L., Pan, D., Pan, D., 2011. Evaluation of retracking algorithms over China and adjacent coastal seas. In: Coastal Altimetry. Springer, Berlin, Heidelberg, pp. 453–471.
Young, I., 1999. Seasonal variability of the global ocean wind and wave climate. Int. J. Climatol. 19 (9), 931–950.
Young, I.R., Babanin, A.V., Zieger, S., 2013. The decay rate of ocean swell observed by altimeter. J. Phys. Oceanogr. 43 (11), 2322–2333.
Yu, Y.-X., Liu, S.-X., Li, Y., Wai, O.W., 2000. Refraction and diffraction of random waves through breakwater. Ocean Eng. 27 (5), 489–509.